CHALMERS
UNIVERSITY OF TECHNOLOGY

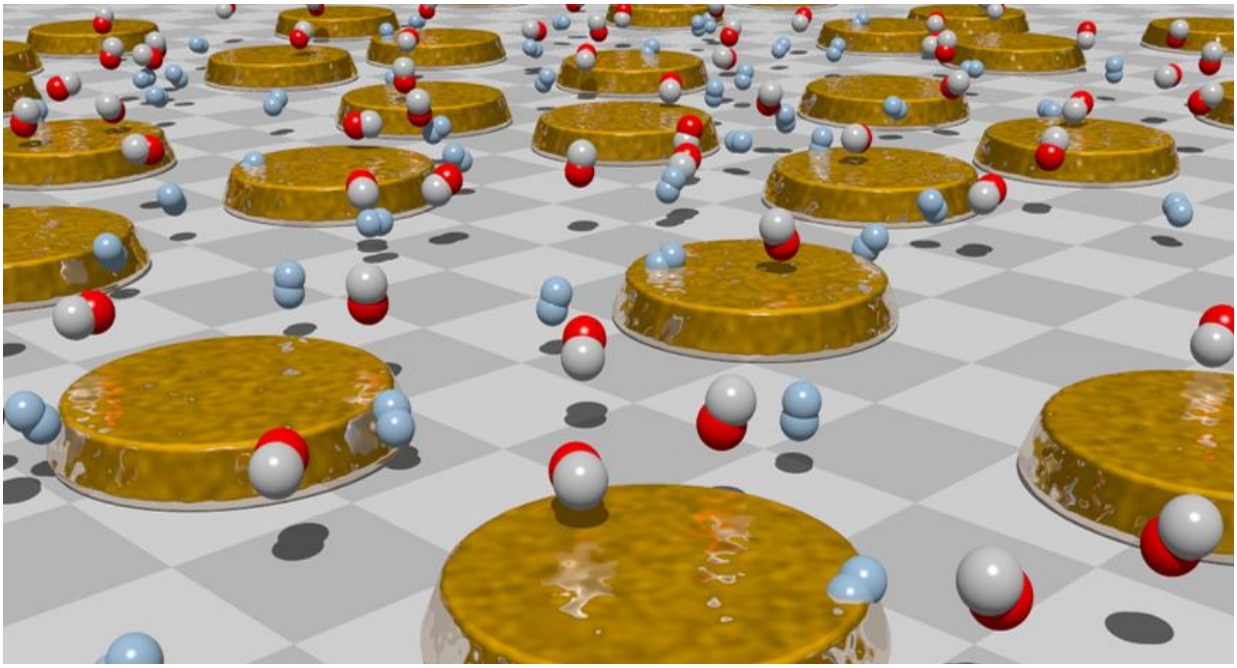

Systematic Study of PdAuCu Alloy Nanoplasmonics for Hydrogen Gas Detection

Master's thesis for M. Sc degree in Nanotechnology Master Program

SARAH ZULFA KHAIRUNNISA

DEPARTMENT OF PHYSICS
DIVISION OF CHEMICAL PHYSICS

CHALMERS UNIVERSITY OF TECHNOLOGY
Gothenburg, Sweden 2020
www.chalmers.se

Thesis for the degree of Master of Science in Nanotechnology

Systematic Study of PdAuCu Alloy Nanoplasmonics for Hydrogen Gas Detection

SARAH ZULFA KHAIRUNNISA

Department of Physics
Division of Chemical Physics
CHALMERS UNIVERSITY OF TECHNOLOGY
Gothenburg, Sweden 2020

Systematic Study of PdAuCu Alloy Nanoplasmonics for Hydrogen Gas Detection

SARAH ZULFA KHAIRUNNISA

Supervisor: Iwan Darmadi, Department of Physics, Chalmers University of Technology, Sweden

Examiner: Christoph Langhammer, Department of Physics, Chalmers University of Technology, Sweden

Department of Physics
Division of Chemical Physics
Chalmers University of Technology
SE-412 96 Gothenburg
Sweden
Telephone + 46 (0)31-772 1000

Cover story:
Illustration of PdAuCu ternary alloy nanoplasmonics for hydrogen gas detection under environment of CO poisoning. Art by Iwan Darmadi.

Printed by: Chalmers Reproservice
Gothenburg, Sweden 2020

Systematic Study of PdAuCu Alloy Nanoplasmonics for Hydrogen Gas Detection

SARAH ZULFA KHAIRUNNISA
Department of Physics, Division of Chemical Physics
Chalmers University of Technology
Gothenburg, Sweden 2020

ABSTRACT

Hydrogen has great potential as an important energy carrier in the future, due to its ability to generate clean and sustainable electricity in a fuel cell. However, hydrogen is flammable even at low concentration (4 vol.%) in ambient air. Furthermore, it is odorless and transparent. Therefore, hydrogen sensors are needed as a warning system for leak detection along the entire value chain.

In this study, I have investigated the composition-dependent response of palladium-alloy-based plasmonic hydrogen sensors. Palladium is of interest due to its inherent selectivity towards hydrogen gas, but it also has inherent disadvantages, such as hysteretic response, and high susceptibility towards CO poisoning. To this end, it has been known that hysteresis and CO-poisoning issues can be addressed by alloying Pd with Au and Cu, and a recent study showed that a ternary alloy (PdAuCu) is able to combine the best features from both PdAu and PdCu binary alloys. However, there is a trade-off between the ternary alloy sensor's sensitivity and CO-poisoning resistance. Therefore, in this thesis, I have systematically screened a broader Cu and Au concentration range in PdAuCu ternary alloys to find the optimum alloyant concentration in this respect.

As the main results, I found that; (i) CO-poisoning resistance is achieved with a Cu content of minimum 15 at.%; (ii) hysteresis-free and linear response is obtained when the Au content is minimum 25 at.%; (iii) the identified champion systems are $Pd_{65}Au_{25}Cu_{10}$ and $Pd_{65}Au_{25}Cu_{15}$, which show reasonably fast response time of 6.8 and 6.1 s; and recovery time of 10.0 and 7.5 s, respectively at room temperature and in synthetic air background for 3.5 % H_2.

Keywords: hydrogen sensor, plasmonic sensing, localized surface plasmon resonance, nanofabrication, hole mask colloidal lithography, hydrogen, palladium hydride, metal nanoparticle alloys.

“The most complete gift of God is a life based on knowledge.”

Imam Ali (as)

PREFACE

It has been a wonderful experience studying in Chalmers University of Technology, Sweden. My study has been financed by the Indonesian Endowment Fund for Education (LPDP) Scholarship.

First and foremost, I would like to thank God and His messengers. Being able to have a journey full of His blessings even though separated from my hometown and family for 10,000 km away. I hope this journey will continue as I continually grow and can benefit the society.

I would like to say thank you to those who have been helpful during the course of the work that have made the research work possible. I would like to thank Christoph Langhammer as my supervisor and examiner for the opportunity in joining his research group and conducting master thesis on the topic I interested in. Also, for the fruitful discussions and valuable suggestions regarding this research and my academic life. Also, to Iwan Darmadi as my daily supervisor and '*kakak lab*', which has taught me since day one to all the materials and devices I was working with and being patient with all the questions and time he has put for me. He contributed a lot in this project. We did it, conquered corona time!

Also thank you for the support during my master study in Chalmers from Chalmers' professors, MC2 staffs, colleagues in the lab (especially Christopher and Johan who gave me more Swedish experience, allowed me to join their Fika at 3 pm) and friends from Nanotechnology Programme (Arimande, Simin, Nooshin, Marne, Joey, Asaad, Zichen, Jakob and David), all of my friends from PPI Gothenburg and PPI Swedia (Bintang, Astrid, Aris, Dhanes, Firman, Budi, Titis, Nurina, mas Iqbaal, mas Ferry) and Chalmers' International Ambassador Team for the great time and experiences. Also, unstoppable moral support from Aksa and my family.

I hope this study can benefit many people, in particular for the hydrogen economy development and as a milestone for me to be a better academia.

Sarah Zulfa Khairunnisa, Gothenburg, 10 June 2020

TABLE OF CONTENTS

LIST OF ABBREVIATIONS

Ar	Argon
CO	Carbon Monoxide
DoE	(US) Department of Energy
e-beam PVD	Electron-beam Physical Vapor Deposition
FWHM	Full-Width of Half-Maximum
H	Hydrogen
HCL	Hole-mask Colloidal Lithography
IPA	Isopropanol
LSPR	Localized Surface Plasmon Resonance
MFC	Mass Flow Controller
mln	Milliliter normal, in STP condition
Mw	Molecular weight
Pd	Palladium
PDDA	Poly (diallyldimethylammonium)
PE RIE	Plasma-Enhanced Reactive Ion Etching
PID	Proportional Integral Derivative
PMMA	Poly (methyl methacrylate)
PS	Polystyrene
sccm	Standard cubic centimeters per minute
%	Volume concentration (L/L) x 10^2
ppm	Volume concentration (L/L) x 10^6
QCM	Quartz Crystal Microbalance

1. Introduction

1.1 Background

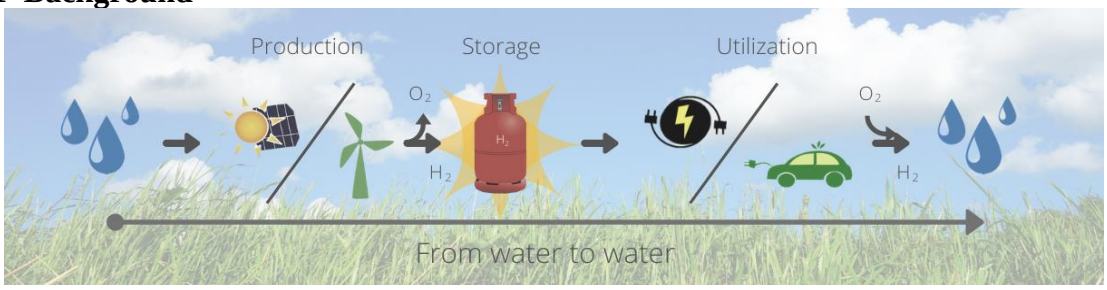

Figure 1.1 Hydrogen economy concept: hydrogen is produced from water by means of a sustainable energy sources (e.g. solar or wind power). The produced hydrogen is stored as energy vector and is used later to generate electricity using a fuel cell. The end product of this electric generation is water.

Clean and sustainable energy production is one of the major global issues nowadays. One of the proposed solutions is the hydrogen economy[1,2] (Figure 1.1). In this scenario, hydrogen gas (H_2) is the energy carrier. On the earth, however, hydrogen does not occur directly as bimolecular gas, but in the form of chemical compounds such as water or hydrocarbons. Therefore, additional attempt has to be done to extract hydrogen gas. Hydrogen production from hydrocarbons exists in several ways *e.g.* steam reforming of natural gas, coal gasification or oxidation of methane. On the other hand, the production from water can be achieved by electrolysis. The production from hydrocarbons, however, is not favorable in terms of sustainability due to its dependence to fossil fuel and its green-house gas product. Thus, in the context of hydrogen economy, electrolysis is more in line. Ideally, water electrolysis is accomplished by means of renewable energy resources (*e.g.* solar or wind energy). The produced hydrogen is then stored as the energy carrier, and in a device known as fuel-cell, hydrogen is utilized to generate electricity (by reaction with oxygen) and releases pure water as the only product. Hence, this cycle *(from water to water)* represents a truly sustainable energy production cycle, which is free from pollutants and green-house gases. This, is in contrast to the conventional fossil fuel based energy system, where CO_2 and other harmful gases, *e.g.* CO, NO_x, SO_x are constantly created, which hampers our ecosystem and health[3].

Hydrogen economy must overcome many technological challenges from different aspects before it is fully implemented, for instance the gas production, storage, transportation, fuel cell efficiency, and safety aspects. The safety aspect of hydrogen gas as energy carrier is critical since hydrogen is flammable when mixed with air even at low concentration (around 4 vol.%) in ambient conditions[3]. Since it is odorless, tasteless and transparent to light at ambient pressure and temperature[4], detection device is needed to detect and monitor unexpected hydrogen leaks.

Table 1.1 Technical requirements of hydrogen safety sensors for automotive and stationary applications[4].

Parameters	Automotive	Stationary
Measurement range	Up to 4 vol.%	Up to 4 vol.%
Detection limit	< 0.1 vol.%	< 0.1 vol.%
Response time	< 1 s	< 30 s
Recovery time	< 1 s	< 30 s
Ambient temperature	-40 to +86°C	-50 to +50°C
Ambient pressure	62-107 kPa	80-110 kPa
Ambient humidity	0-95%	20-80%
Power consumption	< 1 W	-
Lifetime	6000 h	3-5 years
Overall accuracy	± 5% of reading	± 10% of reading

Development of hydrogen detection system has been on going to fulfill the standard sensor requirements. One of the stringent standards is defined by the US Department of Energy (US DoE)[4] (see Table 1.1), where there are ten aspects of sensor qualities to be surmounted. In this project, I focus on the development of the measurement range, detection limit, response/recovery time and accuracy aspects.

In this study, an optical-based detection is utilized, which has advantages such as multiplexing possibility, inherent safety due to lack of electrical contacts, low susceptibility to electromagnetic interference, and possibility for remote sensing[5]. To be more specific, I deployed the localized surface plasmon resonance (LSPR) property of metallic nanoparticle as basis of the hydrogen detection. Moreover, I used Pd nanoparticles, since Pd selectively and spontaneously absorbs hydrogen at ambient conditions. Hydrogen (de)absorption process induces alteration in the LSPR of the Pd nanoparticle, which then is used as sensor readout.

This study is motivated especially by the continuous development of Pd-based nanoplasmonic hydrogen sensor from unary (Pd)[6], binary (PdAu and PdCu)[7] to ternary alloy (PdAuCu)[8]. Unary (single element) Pd nanoplasmonic hydrogen sensors have inherent weaknesses such as hysteresis (leads to ambiguous sensor reading), relatively slow response/recovery time and proneness to poisoning by contaminants such as CO

and sulfuric species[9,10]. Due to this limitations, Wadell *et al.* developed binary PdAu system to suppress the hysteresis via lattice pre-straining[7]. It is reported that hysteresis-free response is achieved when the Au content is at least 25 at.%. They also observed that PdAu alloy enhances the hydrogen sensing response/recovery time compared to the pure Pd counterpart. A PdAu alloy-based sensor, however, is not resistance to CO poisoning, as shown by Darmadi *et al*[8]. They showed that PdCu alloy of as low as 5 at.% promotes resistance to CO poisoning. Despite this excellence, alloying with Cu reduces the sensor's sensitivity. Therefore, the Cu content should be minimized as low as possible without renouncing the CO-protection.

Due to the limitations of PdAu and PdCu, the authors developed a ternary PdAuCu alloy. They showed that PdAuCu of 70, 25 and 5 at. %, respectively exhibits hysteresis-free response and resistance against CO-poisoning, which constitutes the best features of PdAu and PdCu systems. Despite its excellence finding, the study was done for few sets of alloy combinations only. Thus, further systematic investigation of wider range of compositions is required to find the optimized ternary sensor in terms of CO-poisoning resistance, hysteresis-free response and fast response/recovery time. Moreover, the study implemented a rather mild CO-poisoning condition in the testing practice. In this thesis, I develop a harsher CO-poisoning condition to screen the sensor's poisoning resistance, which represents a more realistic scheme.

In this study, the sensor is fabricated using hole-mask colloidal lithography (HCL)[11]. The alloy is achieved by post-fabrication annealing as reported by Nugroho *et al*[9]. The hydrogen test sensing is then conducted using: (i) Insplorion X1 flow reactor for the CO-poisoning tests; (ii) a home-made vacuum chamber for isotherm measurements and; (iii) a mini flow reactor for the fast-kinetic tests.

1.2 Purposes

The purpose of this study is to investigate the optimum alloy composition of the PdAuCu alloy for hydrogen detection according to the CO poisoning resistance, hysteresis-free response and fast response/recovery time.

1.3 Objectives

This study has several objectives such as:

1. Fabrication of PdAuCu alloy nanoparticle arrays with several compositions:
   a. PdCu (1, 3, 5, 7, 10, and 15 at.% Cu).
   b. PdAuCu, with 15 at.% $\leq$ Au $\leq$ 30 at.% and 10 at.% $\leq$ Cu $\leq$ 20 at.%.
2. Hydrogen sensing tests:
   a. Hydrogen sensing tests in CO-contaminant background.
   b. Pressure-optical signal isotherm tests to investigate hysteresis.
   c. Kinetic tests to measure response time and recovery time.
3. Analysis of the obtained sensing results.

2. Theory

The basics principles of hydrogen sensing employed in this project are: (i) localized surface plasmon resonance (LSPR) of metal nanoparticle and (ii) palladium-hydride formation. Therefore, it is imperative to discuss their fundamentals to comprehend the sensor detection mechanism and to rationally optimize the sensor. In this section, I discuss the physical behavior of electrons in metals (Subsection 2.1) as the foundation to the LSPR theory (Subsection 2.2). Later, in Subsection 2.3, I discuss the palladium-hydrogen interaction which covers: the catalytic property of palladium surfaces towards hydrogen gas, thermodynamics of palladium-hydride and palladium alloy-hydride.

2.1 Electrons in Metal

In general, material properties like for example heat and electrical conduction, and the optical properties, can be explained microscopically by its valence electron response towards external intervention. This principle also applies to describe optical properties of metals. Valence electrons in metals are relatively free (compared to semiconductor or insulator), therefore, the electrons can be modeled as an ideal gas. This is the basic assumption of the Drude model[12]. Note that Drude theory turns out to be over simplistic to describe electron-electric field interaction in metals, which leads to development of a more complex theory called Drude-Lorentz theory which adapts non-ideal gas assumptions. But for demonstration and simplification, I used Drude theory to give perspective on the origin of plasmon resonances.

According to the Drude model, the dynamics of one electron in the vicinity of an electric field ($\boldsymbol{E} = \boldsymbol{E_0} e^{-i\omega t}$) is expressed as follows

$$m_e \frac{\partial^2 \boldsymbol{r}(t)}{\partial t^2} + m_e \Gamma \frac{\boldsymbol{r}(t)}{\partial t} = -e\boldsymbol{E_0} e^{-i\omega t}(t) \qquad (2.1)$$

with m_e is effective mass, e is electron charge, and $\boldsymbol{r}$ is electron displacement. The first term of Equation *(2.1)* is the Newton's second law and the second term is the damping effect, defined by Γ (the damping coefficient).

The solution of the above equation can be expressed as displacement of the electron in the frequency domain:

$$\boldsymbol{r}(\omega) = \frac{e}{m_e(\omega^2 + i\Gamma\omega)} \boldsymbol{E}(\omega) \qquad (2.2)$$

For a system with large number of electrons (n), for example in bulk system, the overall dipole moment per unit volume or polarization can be expressed as

$$\boldsymbol{P} = -ne\boldsymbol{r} = \frac{-ne^2}{m_e(\omega^2 + i\Gamma\omega)} \boldsymbol{E} \qquad (2.3)$$

On the other hand, polarization can be also represented as:

$$\boldsymbol{P} = \varepsilon_0(\varepsilon_r - 1)\boldsymbol{E} \qquad (2.4)$$

where ε_0 is permittivity in vacuum and ε_r is the relative permittivity of the electrons.

By comparing Equation *(2.3)* and Equation *(2.4)*, the permittivity can be defined:

$$\varepsilon_r(\omega) = 1 - \frac{\omega_p^2}{(\omega^2 + i\Gamma\omega)} \qquad (2.5)$$

Permittivity of a material (ε_r) represents the susceptibility of the material under the external field (electromagnetic field/light, in this study). When the frequency of the external field (ω) equals to the plasma frequency (ω_p), the free electrons or 'electron gas' oscillates collectively to follow the frequency of the external electromagnetic field. Plasma frequency can be expressed as

$$\omega_p = \sqrt{\frac{ne^2}{m_e\varepsilon_0}} \qquad (2.6)$$

If the electromagnetic wave has frequency higher than the plasma frequency ($\omega > \omega_p$), it will be transmitted since electrons in the material cannot respond fast enough to follow it. On the other hand, if $\omega < \omega_p$, then the electromagnetic field will be reflected just like the case in most metals. That is the reason that metal surface appears to be shiny and reflective.

2.2 Localized Surface Plasmon Resonance (LSPR)

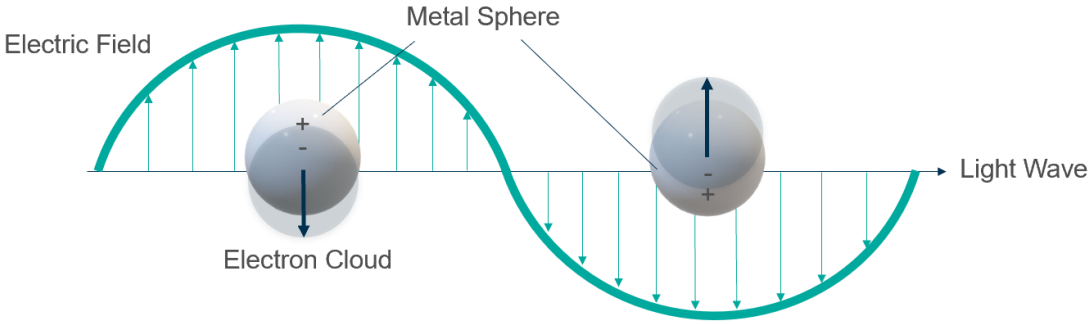

Figure 2.1 Illustration of localized surface plasmon resonance (LSPR) of nano-sized metal sphere. In the resonance condition, the metal's electrons oscillate collectively according to the external electric field of the light.

It has been discussed in the earlier subsection that at plasmon resonance, electrons of the metal follow the frequency of the external driving electric field. However, there is difference in the resonance between bulk and nanosized metal. In the case of bulk metal, the plasmon propagates along the metal surface therefore it is called surface plasmon. In nanosized metal of diameter much smaller than the wavelength of the electric field, the plasma oscillates locally, which inspires the term localized surface plasmon resonance (LSPR) (Figure 2.1).

At the LSPR frequency, metal nanoparticle effectively scatters or absorbs light, represented as a distinct peak in the extinction spectrum and a bright color. A pioneer for the LSPR formalism was a German physicist, Gustav Mie, who solved Maxwell's equations of small particle's interaction with electromagnetic field. In the solution, the particle diameter is assumed to be much smaller than the electromagnetic wavelength (quasi static approximation). The particle-electromagnetic interaction can be represented by the extinction (σ_{ext}), absorption (σ_{abs}) and scattering (σ_{sca}) cross-section. For a sphere-shaped particle, those cross-sections are expressed as:

$$\sigma_{ext} = \frac{18\pi\varepsilon_m^{3/2}V}{\lambda} \frac{\varepsilon_2(\lambda)}{[\varepsilon_1(\lambda)+2\varepsilon_m]^2+\varepsilon_2(\lambda)^2} \quad (2.7)$$

$$\sigma_{sca} = \frac{32\pi^4\varepsilon_m^2V^2}{\lambda^4} \frac{(\varepsilon_1-\varepsilon_m)^2+(\varepsilon_2)^2}{[\varepsilon_1(\lambda)+2\varepsilon_m]^2+\varepsilon_2(\lambda)^2} \quad (2.8)$$

$$\sigma_{abs} = \sigma_{ext} - \sigma_{sca} \quad (2.9)$$

Where ε_1 and ε_2 are real and imaginary dielectric function parts of the metal, respectively, λ is the light/electromagnetic wavelength, ε_m is permittivity of the surrounding medium and V is the particle's volume. From the above equations, it can be concluded that particle-light interaction is highly dependent on two things, the dimension (V) and surrounding medium (ε_m). In sensor application, this insight is useful for the material design to achieve an optimized sensor.

From the equations above, the dependence of the particle-light interaction to the surrounding medium can be calculated as follows:

$$\lambda_{LSPR} = \lambda_p\sqrt{1+2n^2} \quad (2.10)$$

where λ_{LSPR} is the LSPR frequency, λ_p is the plasma resonance of the bulk and n is the relative refractive index of the medium.

In the case of hydrogen detection using Pd nanoparticle, the LSPR shift is enabled by the distinct permittivity contrast between Pd and Pd-hydride[13] and to lesser-extend the volume difference between the two.

2.3 Pd-Hydride

The main reason of using Pd as the host material is due to the selectivity of Pd towards hydrogen. Pd selectively catalyzes the dissociation of hydrogen gas on the surface and absorbs the dissociated atomic hydrogen into the lattice to form a hydride. Hydride formation is not exclusive to Pd, other materials *e.g.* Hf, Y, Mg, Ta, V are also known to form hydrides with larger optical contrast but they suffer from extremely slow (de)absorption time and are not able to dissociate molecular hydrogen at ambient condition (thus a Pd capping layer is required)[14].

2.3.1 Pd and Hydrogen Molecule Interaction

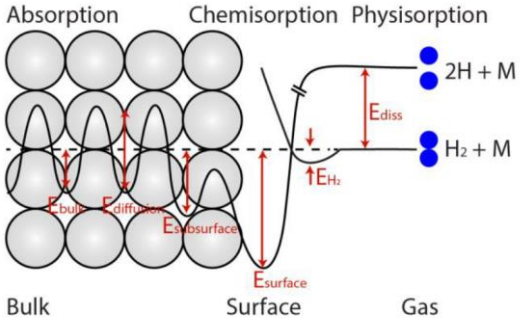

Figure 2.2 Schematic of energy landscape encountered by hydrogen molecule near a Pd surface on its way into the bulk (figure is from[14], adapted from[15]). Numerous stages are shown in the schematic: E_{H_2} corresponds to the physisorption energy of H_2 molecule. E_{diss} is the required energy to dissociate hydrogen from bimolecular to atomic form. The dissociated hydrogen chemisorbed spontaneously on the Pd surface, indicated by the negative activation energy on the surface ($E_{surface}$). En route from surface to

the bulk, the hydrogen has to overcome numerous energy barriers at subsurface ($E_{subsurface}$) and at bulk (E_{bulk}) interstitial sites. $E_{diffusion}$ corresponds to the activation energy of hydrogen diffusion into the bulk.

The absorption of hydrogen atoms into Pd bulk is preceded by the hydrogen molecule interaction with the metal surface. Within an atomic distance, the hydrogen molecule (H_2) is dissociated into atomic hydrogen by the Pd surface. The dissociation of hydrogen molecules on the Pd surface occurs spontaneously at ambient conditions, *i.e.* without activation barrier[14] (Figure 2.2). Later, the atomic hydrogen diffuses into the bulk by overcoming diffusion energy barriers at subsurface and bulk interstitial site positions. These energy barriers determine the hydrogen absorption time.

In the case of desorption, the reverse process occurs where the hydrogen atom diffuses towards the surface and recombines to form bimolecular H_2 before it is desorbed from the Pd surface, with the associative desorption being the rate-limiting step[16].

2.3.2 Thermodynamics of Palladium-Hydride Formation

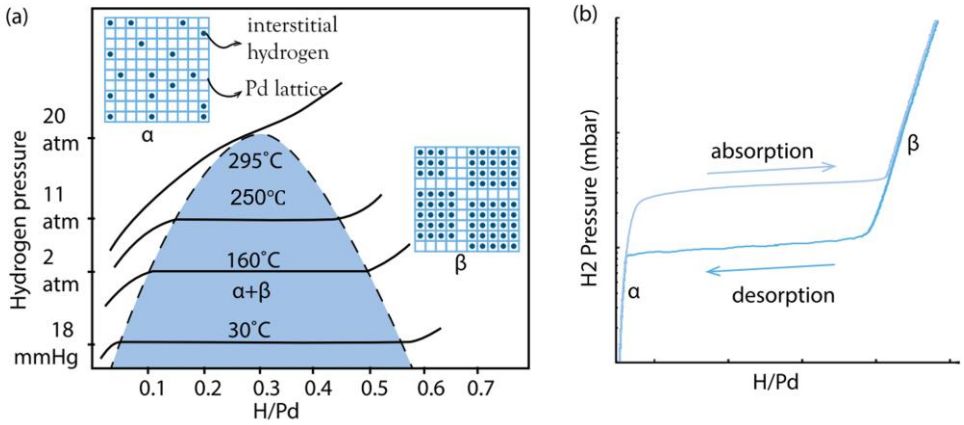

Figure 2.3 (a) Hydrogen absorption pressure-composition isotherms for different temperatures and correspondingly obtained Pd-H phase diagram and (b) room-temperature isotherm of hydrogen ab/desorption that exhibits hysteresis. Figure is taken from[17], adapted from[18].

There are three stages of hydrogen absorption into Pd, depending on the partial hydrogen pressure (see Figure 2.3). At low hydrogen pressure, the amount of interstitial hydrogen is very low and therefore hydrogen-hydrogen interaction is weak. This phase corresponds to α-phase, where hydrogen is in a so-called solid solution. In this phase, the hydrogen content in the Pd lattice correlates linearly to the square root of the hydrogen partial pressure:

$$\sqrt{P_{H_2}} = n_H K_S \qquad (2.11)$$

This correlation is known as Sievert law, where P_{H2} is the partial pressure of hydrogen gas, n_H is the hydrogen concentration in metal (in this case Pd) and K_S is the Sieverts constant.

With increasing hydrogen partial pressure, hydrogen concentration in Pd grows, and due to long-range H-H interactions mainly mediated by lattice strain, clusters of hydride β-phase start to form. In between the α- and β- phases,

across the first-order transformation, there is a mixed α + β phase, represented by a plateau in the pressure-composition isotherm. The introduction of hydrogen to the Pd lattice consequently expands the lattice. At β-phase, the lattice constant of Pd increases from 3.89 Å to 4.03 Å[19].

It is worth noting that there is a certain temperature where the plateau and hysteresis disappear, which implies that the phase transformation is no longer first-order. This temperature is known as critical temperature T_c, which is 295°C for bulk Pd[18].

Another inherent feature of Pd hydride formation/decomposition is hysteresis, which refers to different absorption and desorption routes in the pressure-composition isotherm (Figure 2.3b). The hysteresis is a consequence of different lattice-strain induced energy barriers that need to be surmounted when the hydride is formed or decomposed[20]. As a consequence, plateau pressure in the absorption is higher than that of the desorption.

In the context of hydrogen sensing applications, hysteresis is a disadvantage because the sensor readout will be ambiguous and depends on the sensor history. To overcome hysteresis, there are at least two strategies: (i) to increase the operational temperature above T_c[21,22] and (ii) to alloy Pd with metal of different lattice constant.

2.4 Pd-Alloy Hydride

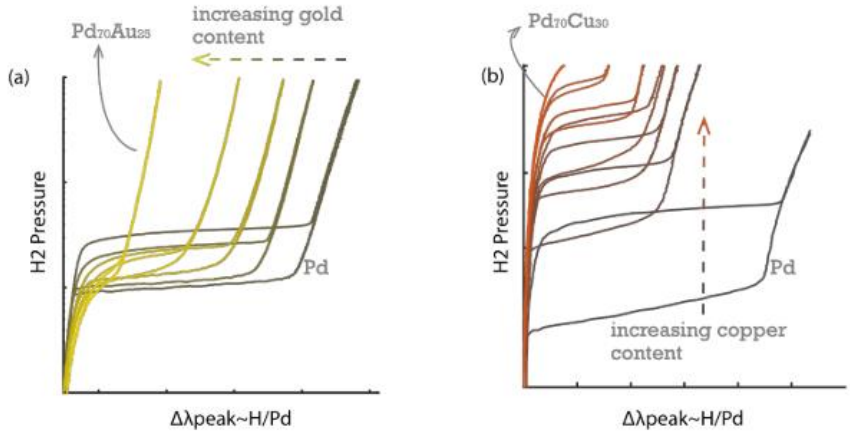

Figure 2.4 Hydrogen pressure-LSPR peak shift ($\Delta\lambda_{peak}$) isotherms of (a) PdAu and (b) PdCu binary alloy systems. The two systems show different isotherm trend with increasing alloyant concentration. The isotherms were obtained at 30°C in the 1-1000 mbar hydrogen pressure range (the figure was adapted from[17]).

Hysteresis-free isotherm can be achieved by alloying Pd with another miscible metal for example Au and Cu. As shown in Figure 2.4, the alloyant concentration clearly affects the isotherms of PdAu and PdCu. In the case of PdAu, addition of Au reduces the hysteresis gap by lowering the absorption plateau and raising the desorption plateau. When the Au concentration is at least 25 at.%, the hysteresis disappears. The hysteresis disappearance is consequence of lattice pre-straining due to larger Au lattice constant compared to that of Pd (3.884 Å[23] vs 4.078 Å[24]).

For the PdCu system, the hysteresis suppression appears differently than for the PdAu system. With increasing Cu content, both absorption and desorption plateaus elevate

towards higher pressure. At Cu 30 at.%, the isotherm is completely in the α-phase and hysteresis free within the 1-1000 mbar pressure range at 30°C (Figure 2.4b). While Au expands the Pd lattice due to its larger atomic radius, Cu shrinks it because the Cu atoms are smaller. Consequently, the Cu lattice constant is smaller than that of Pd (a = 3.627 Å[25]).

3. Nanofabrication Methods

Nanoparticles can be made via two different principles/routes: bottom-up and top-down. As the name suggests, the bottom-up route develops a nanostructure starting from a smaller entity that assembles towards larger structure according to the thermodynamics and kinetics. An example of this route is colloidal synthesis. On the other hand, the top-down route implements physical or chemical treatment to break macroscopic entity down into nanometer scale. Examples of this route are e-beam lithography and ball-milling. Each of the routes has its own advantages and disadvantages. The bottom-up is generally superior in the scalability and the versatility to produce sophisticated nanoparticle shapes/facets while often problematic in yield and reproducibility. The top-down, on the other hand, is advantageous for the yield, reproducibility and possibility to arrange nanoparticles within a well-defined array on a surface but inferior in terms of scalability due to the need of serial-made masks.

With the limitation of both routes, the hole-mask colloidal lithography (HCL) method was developed by Fredriksson *et al*[11]. The HCL method is a hybrid between bottom-up and top-down since it utilizes colloidal polystyrene (PS) nanobeads, which self-assemble on a substrate to form a mask subsequently used for lithographic patterning. The PS nanobeads are charged, thus the repulsive force leads to self-assembled quasi-random nanobeads array. The PS nanobeads determine the size, composition, and shape of patterned nanoparticles. HCL is versatile because it is in principle can be adopted to any materials. Furthermore, the method enables nanoparticles patterning on a vast surface area, thanks to the self-assembly based process used to make the patterning mask.

For these considerations, HCL is used to prepare the hydrogen sensor samples. In this section, the sample preparation method is explained step-by-step and as a sidetrack, the employed techniques' working principles are also discussed. The HCL fabrication section is organized as follows: (i) mask preparation (from spin coating to plasma reactive ion etching) in Subsection 3.1, (ii) material deposition and mask lift-off in Subsection 3.2, and (iii) annealing in Subsection 3.3.

3.1 Mask Preparation

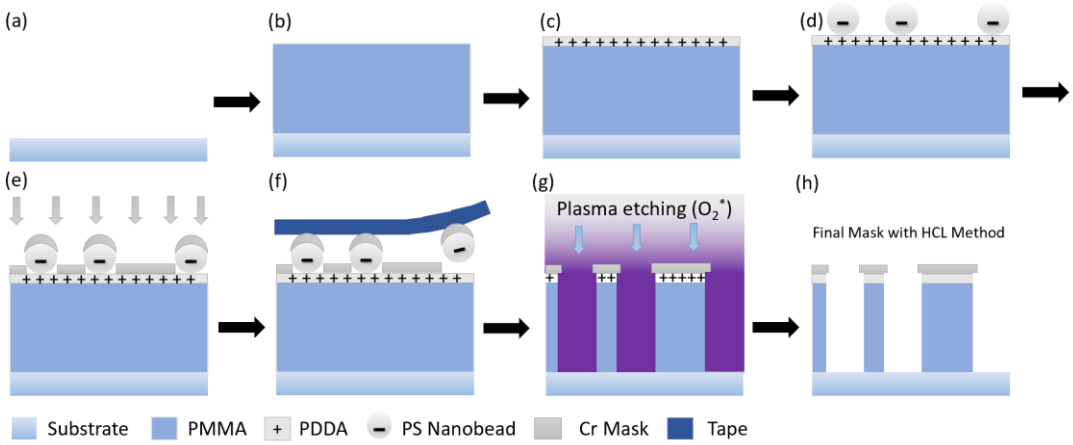

Figure 3.1 Hole-mask colloidal lithography (HCL) nanofabrication scheme: (a) Cleaned fused silica as substrate, (b) PMMA spin coating, (c) PDDA drop coating, (d) PS solution drop coating, (e) Cr deposition, (f) tape stripping, (g) oxygen plasma dry etching, and (h) final mask.

The Pd and Pd-alloy nanoparticles are patterned on a fused silica substrate (thickness 0.5 mm). This transparent substrate enables transmission-mode LSPR monitoring. All the fabrication was done in Chalmers cleanroom facility. The mask preparation is illustrated in Figure 3.1 and followed these steps:

a. The substrate was cleaned by sonication (Powersonic P230D) using IPA, acetone and methanol subsequently for one minute. Later, it was dried by nitrogen gas blow. The cleaning ensures that the substrate is free from dust or other contaminants (Figure 3.1a).

b. The spin coating process started with mounting the fused silica substrate on the rotator followed by drop coating of anisole diluted poly (methyl methacrylate) (PMMA) solution on the substrate. The PMMA solution was obtained from Microchem AB (A4, Mw = 950 000). The spin coating was done with 2000 (rpm) angular speed and 1000 ($1/s^2$) acceleration for 30 seconds (Figure 3.1b).

   After the spin coating, the sample was soft-baked on a hot-plate to remove the solvent. The baking temperature was 150°C for 3 minutes. This temperature is above solvent boiling point to ensure complete evaporation. The final polymer thickness is expected to be around 300 nm.

c. A short (5s) oxygen plasma etch was carried out (50 W, 250 Torr, 10 sccm) to reduce the PMMA hydrophobicity before PDDA (Mw 100 000-200 000 diluted in 20% H_2O to achieve 0.2 wt.% concentration) was drop cast. The PDDA was incubated for 40 seconds and then rinsed with Milli-Q water for 10 seconds to remove the excess PDDA. Afterwards, nitrogen blow dry was applied. The PDDA serves as positive-charged layer to keep the negatively charged polystyrene (PS) nanobeads to PMMA surface (Figure 3.1c).

d. PS nanobeads solution (negatively charged, diluted in Milli-Q water to 0.2 wt.% concentration, average size 190 nm) was drop cast and incubated for 2.5 minutes. The PS nanobeads self-assembled on the surface to form a quasi-random array. Subsequently, the excess solution was removed by 10 seconds rinsing with water followed by nitrogen blow dry (Figure 3.1d).

e. A Cr layer of 150 Å thickness was deposited using Kurt Lesker e-beam physical vapor deposition (PVD) with 5×10^{-7} Torr base-pressure, 9 kV electron gun power and 1 Å/s deposition rate (Figure 3.1e). This give resistant to reactive oxygen plasma etching.

f. The Cr-covered PS nanobeads were removed by tape-stripping (Nitto Adhesive Tape) leaving holes of exposed PMMA (Figure 3.1f).

g. Finally, oxygen plasma etching (50 W, 250 Torr, 5 minutes, 10 sccm, PlasmaTherm Batchtop) was applied to remove PMMA sacrificial layer on the exposed hole (Figure 3.1g). The final mask structure is shown in (Figure 3.1h).

3.2 Material Deposition and Mask Lift-off

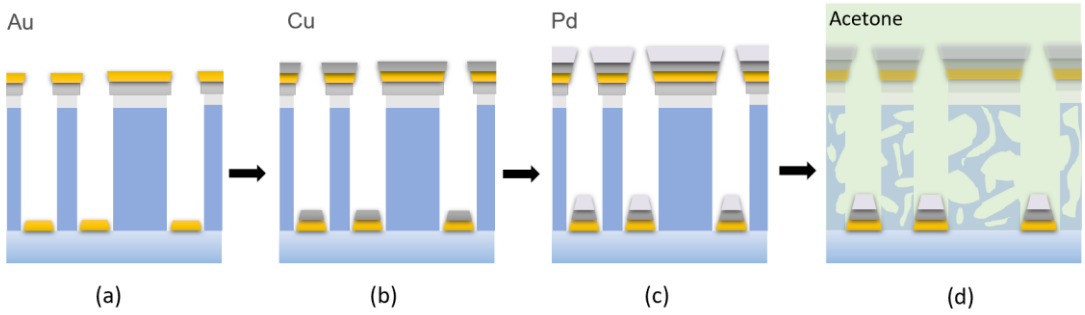

Figure 3.2 Material depositions and mask lift-off. The constituent materials, in this case Au, Cu, and Pd are deposited subsequently (a → c). (d) Mask lift-off process by immersing the sample into acetone solution to dissolve the PMMA sacrificial layer.

The next step after mask preparation is the material deposition. The alloy nanofabrication process starts by subsequent depositions of the constituent materials resulting in a multilayer nanodisks (Figure 3.2a-c). The thickness of each layer determines the relative concentration of the alloyant. In this study, two set alloys were prepared in the form of the binary PdCu system and the ternary PdAuCu system.

Later, the mask and the sacrificial layer were removed with acetone, leaving arrays of multilayer nanodisks on the substrate (Figure 3.2d).

3.3 Annealing

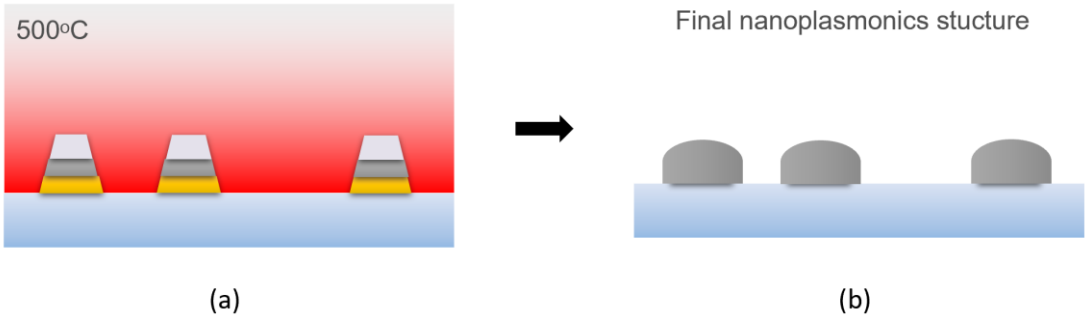

Figure 3.3 (a) Annealing of the fabricated nanodisks array to promote the alloying (b).

In the final step, a high temperature treatment was applied to the prepared multilayer nanodisks to promote the alloy formation (see Figure 3.3). Annealing was carried out in reducing atmosphere (4% H_2 in Ar at 200 mln/min), at 500°C for 24 hours to ensure homogenous alloy formation[7,9]. Reducing gas is necessary to avoid unwanted oxide formation.

4. Nanofabrication Techniques

In this chapter, I discuss the nanofabrication techniques I used to fabricate the sensor: (i) spin coating, (ii) plasma dry etching and (iii) e-beam physical vapor deposition.

4.1 Spin Coating

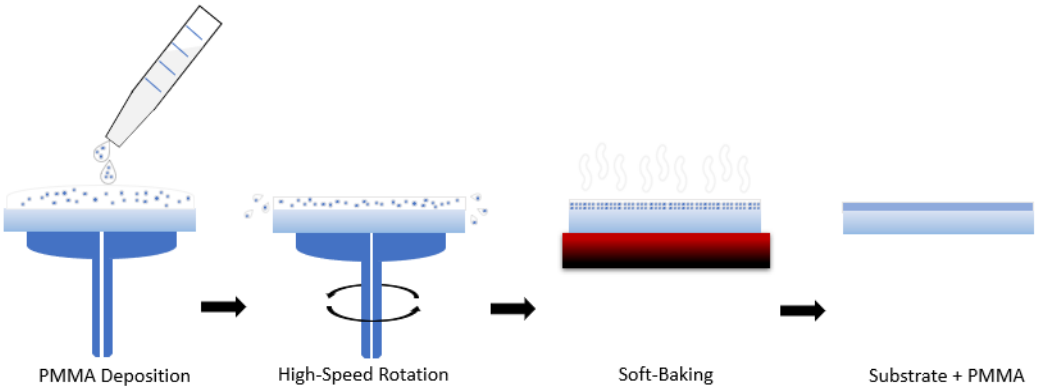

Figure 4.1 Spin coating and soft baking processes. Polymer (in this case PMMA) solution is dropped on a solid substrate (fused silica), which is mounted on the rotator. The spin coating is followed by soft baking on the hot plate to evaporate the polymer solvent.

Spin coating is a technique to deposit a thin film layer on a solid substrate by means of centrifugal force (illustrated in Figure 4.1). This technique is possible if the desired material can be diluted in a certain solvent. Soft baking is a necessary additional step to remove the excess solvent. The advantage of spin coating is the ability to produce uniform films rapidly on a large area.

The film thickness (t) is determined by the angular spin speed (ω) as $t \propto 1/\sqrt{\omega}$[26,27]. In this project, the spin coating was utilized to deposit PMMA layer as *a sacrificial layer* for the HCL nanofabrication described above.

4.2 Plasma Dry Etching

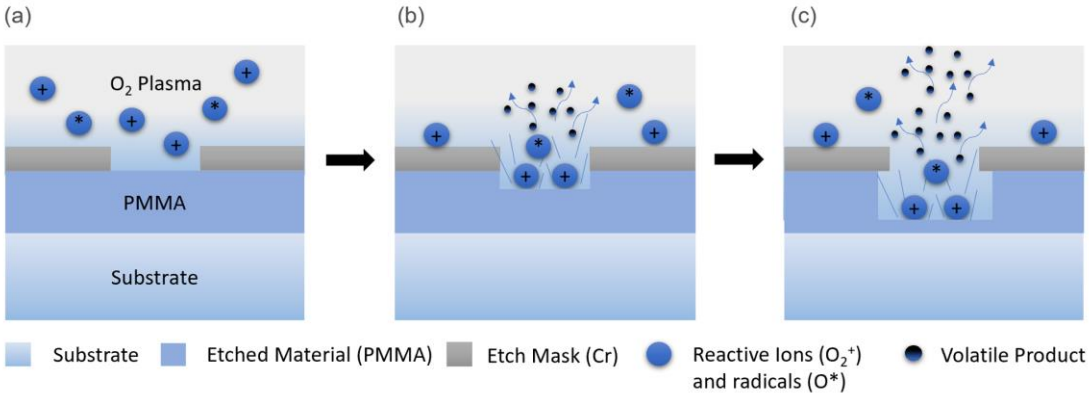

Figure 4.2 Plasma dry etching process to remove PMMA using oxygen plasma. (a) Plasma induces formation of ions (O^+) and radicals (O). (b) Due to the voltage bias between the plasma and the substrate, the ions (O^+) are accelerated towards the substrate and impinge on the PMMA. On the other hand, the radicals (O*) are chemically reactive to PMMA yielding volatile water, carbon monoxide, carbon dioxide, and hydrocarbon compounds.*

Plasma is a state of matter comprised of a mixture of electrons, ions, excited molecules/atoms, and neutral particles[28]. One way to generate plasma is by

subjecting gas to high electric field, which results in separation of positive and negative charges while maintaining zero net charge. The generated plasma then induces formation of radicals, which are reactive to target material. The radicals react with the target material yielding volatile products. This constitutes the chemical process of the etching. On the other hand, voltage bias between the plasma and the target material leads to transfer of ions from the plasma to the target material. Due to the high kinetic energy, these accelerated ions knock out the target material out via ballistic collision (Figure 4.2). Thus, etching process is actually a combination of chemical and physical processes. However, in etching process I used, the physical process is much less compared to the chemical process.

4.3 Electron-beam Physical Vapor Deposition (e-beam PVD)

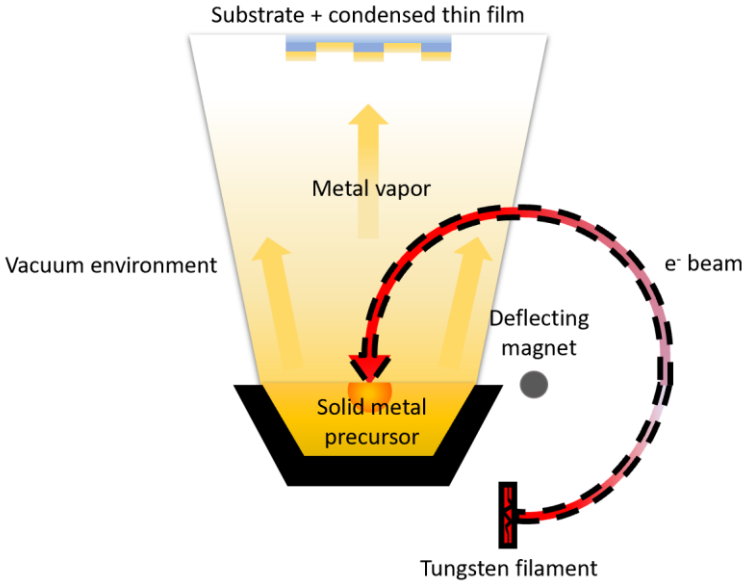

Figure 4.3 Electron-beam physical vapor deposition process: solid metal in a crucible is evaporated by heating it via impinging high-energy electrons. The electrons are guided by a magnetic field from a heated tungsten filament to the crucible. The evaporated material condensates on the substrate.

The schematic of e-beam physical vapor deposition is presented in Figure 4.3. Electrons are generated by a tungsten filament via resistance heating. The generated electrons are guided by a magnetic field trough a circular path to the target material located at positive electrode. The high energy electron beam heats the target such that evaporation takes place and metal species travels through the vacuum chamber to the sample substrate. Upon the impact on the substrate, the evaporated materials nucleate and grow into a thin film layer.

5. Hydrogen Sensing Tests

In this project, three setups for hydrogen sensing tests were used: (i) Insplorion X1, (ii) vacuum chamber setup, and (iii) mini-chamber flow reactor. Insplorion X1 was utilized to test the sensing in a synthetic air background with CO contaminant. The vacuum chamber setup was employed to study the pressure-composition isotherm of the prepared sensor. Mini-chamber flow reactor was used to measure kinetics (response time and recovery time) in realistic environments.

5.1 Insplorion X1 Flow Reactor

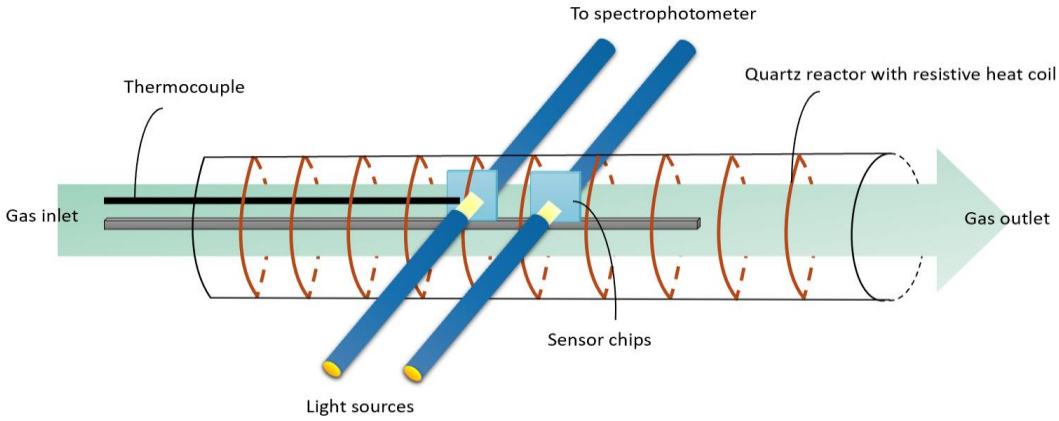

Figure 5.1 Insplorion X1 flow reactor.

The schematic of the Insplorion X1 flow reactor is presented in Figure 5.1. The reactor chamber is a quartz tube, which enables optical monitoring of the sensor. The sample is illuminated by a light source (Avantes AvaLight-Hal) via an optical fiber (Avantes FCB-IR600-2) and an optical collimator. On the other side of the reactor, transmitted light is collected by the second collimator and optical fiber connected to a UV-visible range spectrophotometer (Avantes SensLine AvaSpec-2048). The reactor supports parallel measurement of two samples. The spectral data acquisition is done by Insplorer software. The data-fitting is performed in real-time to yield the optical descriptors (*i.e.* plasmonic peak position, centroid, full-width of half-maximum/FWHM, and extinction).

The quartz reactor is wrapped with a resistive heating coil, which is connected to a DC power supply (Delta Elektronika SM18-50). The power supply is controlled by a PID thermocontroller (Eurotherm 3216) in a feedback-loop scheme using in-reactor thermocouple as input. The operational temperature was set to 30°C.

The gas flow through to the reactor is controlled using MFCs (Bronkhorst ΔP). In this project, three MFCs (each connected to either Ar or synthetic air, 10% CO in Ar, and 25% H_2 in Ar reservoirs, respectively) were used to control the CO and H_2 concentrations in Ar or synthetic air carrier gas. The total gas flow rate is 200 ml/min.

5.2 Vacuum Chamber

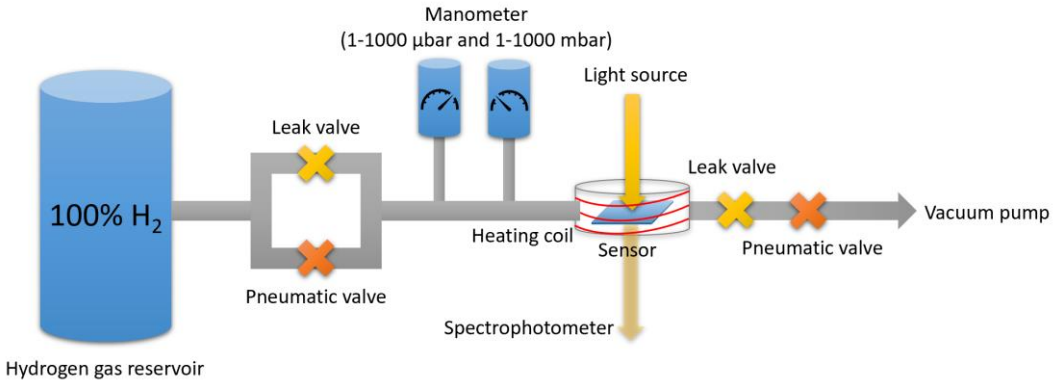

Figure 5.2 Schematic of the vacuum chamber.

The schematic of vacuum chamber for pressure-composition isotherm measurement is shown in Figure 5.2. The vacuum chamber is equipped with two sapphire vacuum view ports, which enables transmission-mode monitoring of the sensor. The sensor is illuminated from one viewport by a polychromatic halogen light source (Avantes AvaLight-Hal) guided by an optical fiber and a light collimator. The transmitted light is collected from the other viewport by a UV-visible fixed-grating spectrophotometer (Avantes SensLine AvaSpec) via an optical fiber and collimator.

The vacuum chamber is wrapped with a resistive heating coil connected to a DC power supply. The sample temperature is monitored using a thermocouple wire, which is in contact with the sample. The DC power supply is controlled by a PID thermocontroller (Eurotherm 3216) in a feedback-loop manner with the thermocouple. The pressure-composition isotherms were measured at 30°C.

A 100% hydrogen reservoir is separated to the reactor by a leak valve and a pneumatic valve, which are connected in parallel. The other side of the reactor is connected to a turbo vacuum pump (Pfeiffer Turbomolecular Pump) separated by a serial connected leak and pneumatic valve. The leak valves are the crucial parts in the isotherm measurement, which requires a quasi-static pressure. The chamber pressure is monitored with two capacitance manometers (MKS PDR2000 Baratron) of different resolution: 1-1000 µbar and 1-1000 mbar.

5.3 Mini Chamber Flow Reactor

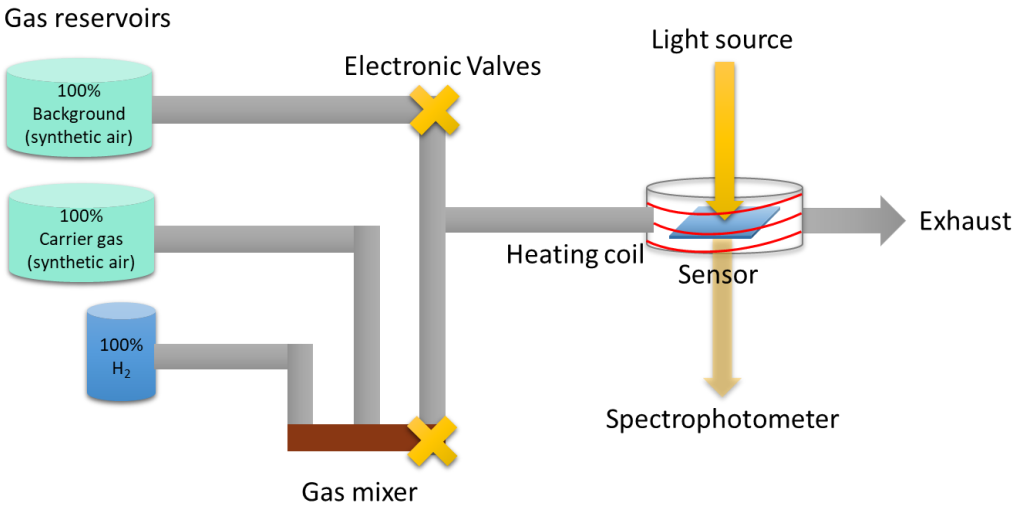

Figure 5.3 Schematic of the mini chamber flow reactor.

The schematic of mini chamber flow reactor is presented in Figure 5.3. Basic principle of this reactor is the same as for the Insplorion X1 flow reactor (Subsection 5.1). The main difference is the small chamber volume and the fast-electronic valves. The small reactor is designed to eliminate long diffusion time of the gas to reach the sensors. The fast-electronic valves enable fast switching between hydrogen and the background gas. Similar to the vacuum system, the heating system was operated in a feedback-loop manner and the optics monitoring was done in transmission-mode.

The hydrogen concentration and the total gas flow were controlled using three MFCs (Bronkhorst ΔP). For the kinetic test, the hydrogen concentration was kept at 3.5 vol.% in a total flow of 200 ml/min with operational temperature at 25°C.

6. Results and Discussions

6.1 Finding Minimum Cu for CO Resistance

It is worth to mention again that alloying Pd with Cu leads to competing effects between the CO-poisoning resistance and the sensor sensitivity[8]. The increasing concentration of the Cu alloyant improves the sensor's CO resistance, while it reduces the sensitivity. Therefore, it is imperative to investigate the minimum concentration of the Cu alloyant that is sufficient for the CO-poisoning resistance to minimize the sensitivity decline.

For this investigation, I prepared the binary PdCu alloys of increasing concentrations: 1, 3, 5, 7, 10 and 15 at.%. The test protocol is shown in Figure 6.1 (b), where the sensor was exposed to 3 × 3 vol.% H_2 pulses as the control before the CO background was introduced. This protocol is in contrast to that in Darmadi *et al.*'s work[8] (Figure 6.1 (a)), where the CO contaminant was introduced only during the H_2 pulses. The protocol I proposed here is more relevant for real applications since the sensor can be exposed to CO contaminant before H_2 exposure and the CO contaminant might persist for indefinite time. Furthermore, 3 vol.% concentration of H_2 is used to avoid Pd's absorption plateau pressure (at 4 vol.%) where the signal is unstable.

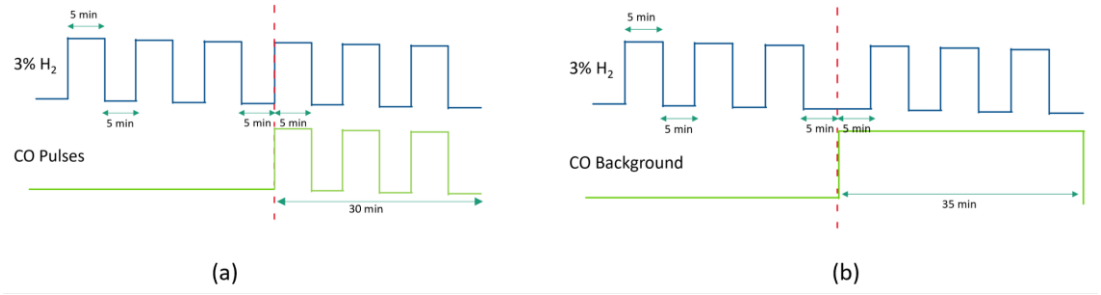

Figure 6.1 Two different protocols of the CO-poisoning test: (a)the CO-contaminant is introduced as a short pulse simultaneously with the H_2 pulse. This protocol is adapted in Darmadi et al.'s study[8]. (b) the CO-contaminant is introduced as background. The second protocol is used in this thesis.

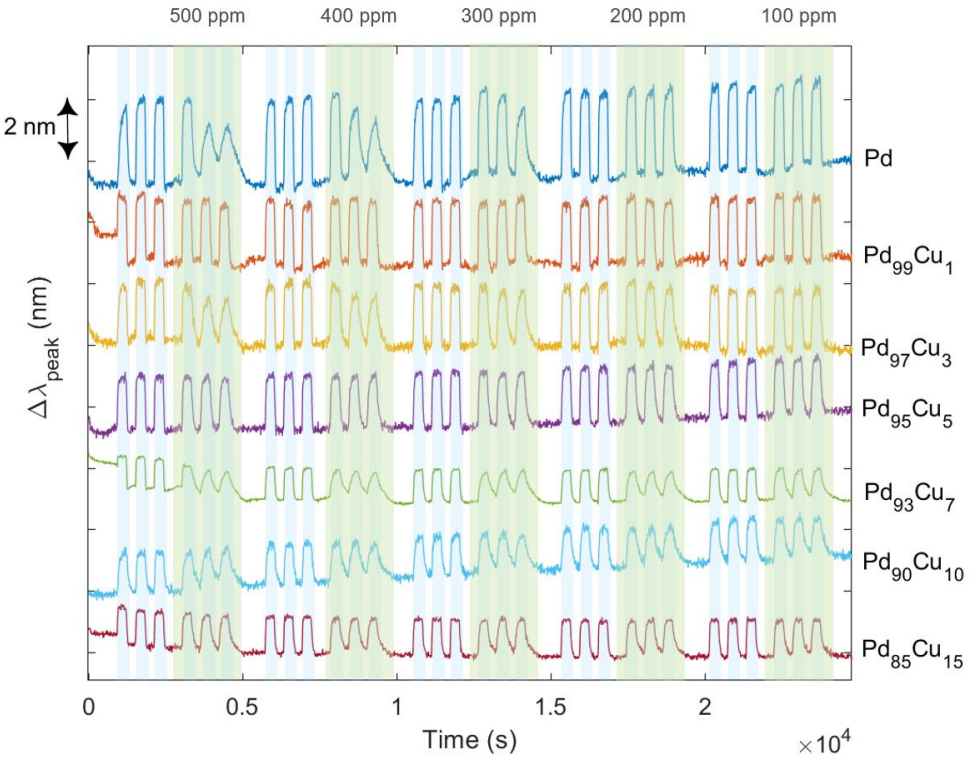

Figure 6.2 The LSPR peak position shift ($\Delta\lambda_{peak}$) of the PdCu-alloy sensors to 3 vol.% H_2 pulses in synthetic air carrier with changing CO concentration background. Blue-shaded and turquoise-shaded areas correspond to H_2 and CO pulses, subsequently.

The LSPR peak position shifts ($\Delta\lambda_{peak}$) of the PdCu-alloy sensors towards 3 vol.% H_2 pulses in various CO background is presented in Figure 6.2. The descending CO concentration backgrounds were 500 ppm, 400 ppm, 300 ppm, 200 ppm and 100 ppm.

There are several interesting observations to highlight:

(i) It is obvious that the alloy of higher Cu concentration shows smaller $\Delta\lambda_{peak}$, which is consistent with Darmadi *et al.*'s finding[8]. The shift or sensitivity is consequence of the lower amount of Pd in the higher Cu-concentration alloys. It has been shown recently that in alloy, only Pd absorbs hydrogen[29]. Another explanation of the decreasing sensitivity is that Cu shrinks the Pd lattice such that it increases the required energy to add more hydrogen into the lattice[30].

(ii) It can be clearly seen that the higher CO concentration leads to slower kinetics as indicated by the unsatured responses. It is not so surprising because the higher CO concentration leads to higher CO adsorption *i.e.* poisoning on the nanodisk's surface. It is interesting that in case of pure Pd, the sensor is still tolerant to 200 and 100 ppm CO concentration, indicated by the saturated absorption and desorption. This excellent tolerance at the considerably high concentration CO could have been assisted by the synthetic air background[31]. Pd is known to have catalytic effect that oxidizes CO in presence of O_2[31].

(iii) In 500 ppm CO, Pd kinetics are severely slowed down by the CO poisoning. In this CO concentration, it is evident that Cu alloying minimizes the poisoning effect. The $Pd_{99}Cu_1$, $Pd_{95}Cu_5$, and $Pd_{85}Cu_{15}$ showed tolerance towards this CO concentration, as indicated by the saturated absorption and desorption for all three pulses. It is interesting that alloys of Cu concentration as low as 1 and 5 at.% are resistant to the poisoning. One of the speculations is that the actual Cu concentration on the alloy surface is actually higher than the bulk, which consequently enhances the poisoning resistance.

(iv) The CO poisoning effect is reversible in the tested concentrations. All of the sensors recover immediately after the CO background is removed and subsequently flushed with the synthetic air for 5 min.

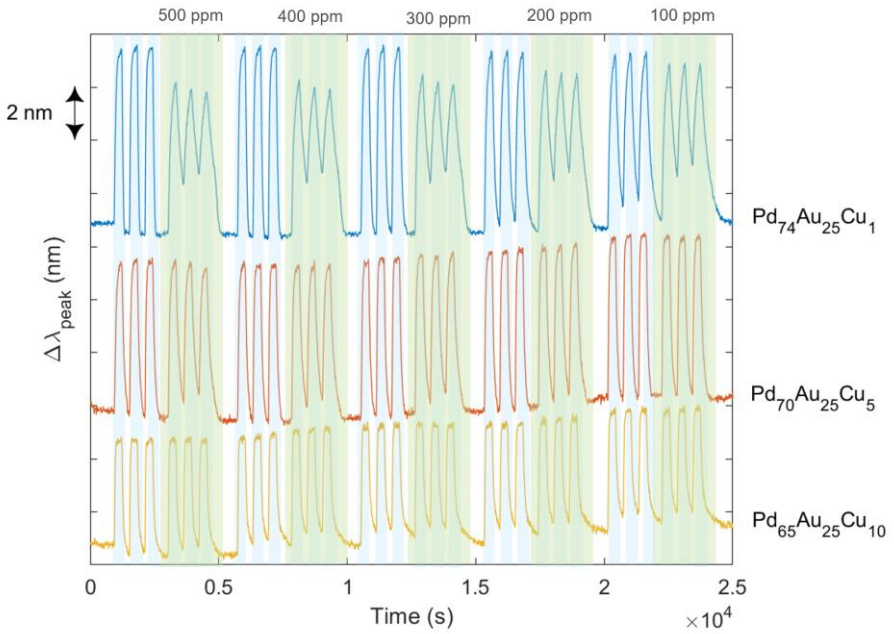

Figure 6.3 The LSPR peak position shift ($\Delta\lambda_{peak}$) of the PdAuCu-alloy sensors with 1 at.%, 5 at.% and 15 at.% Cu in order to test CO poisoning resistant.

As a follow up of the remarkable tolerance of $Pd_{99}Cu_1$ and $Pd_{95}Cu_5$ in the tested CO background (Figure 6.2), I introduced 1 and 5 at.% Cu in the ternary alloys as $Pd_{74}Au_{25}Cu_1$ and $Pd_{70}Au_{25}Cu_5$. These alloys are then tested in the similar tested to that in Figure 6.2. In contrast to the binary PdCu system, I found that 1 and 5 at.% Cu did not sufficiently promotes the tolerance in the 500 ppm CO (Figure 6.3). Furthermore, I found that at least 10 at.% is necessary to induce the CO tolerance. Therefore, for the isotherm optimization later, I utilize at least 10 at.% Cu.

6.2 Absorption and Desorption Time Dependence on Cu Concentration

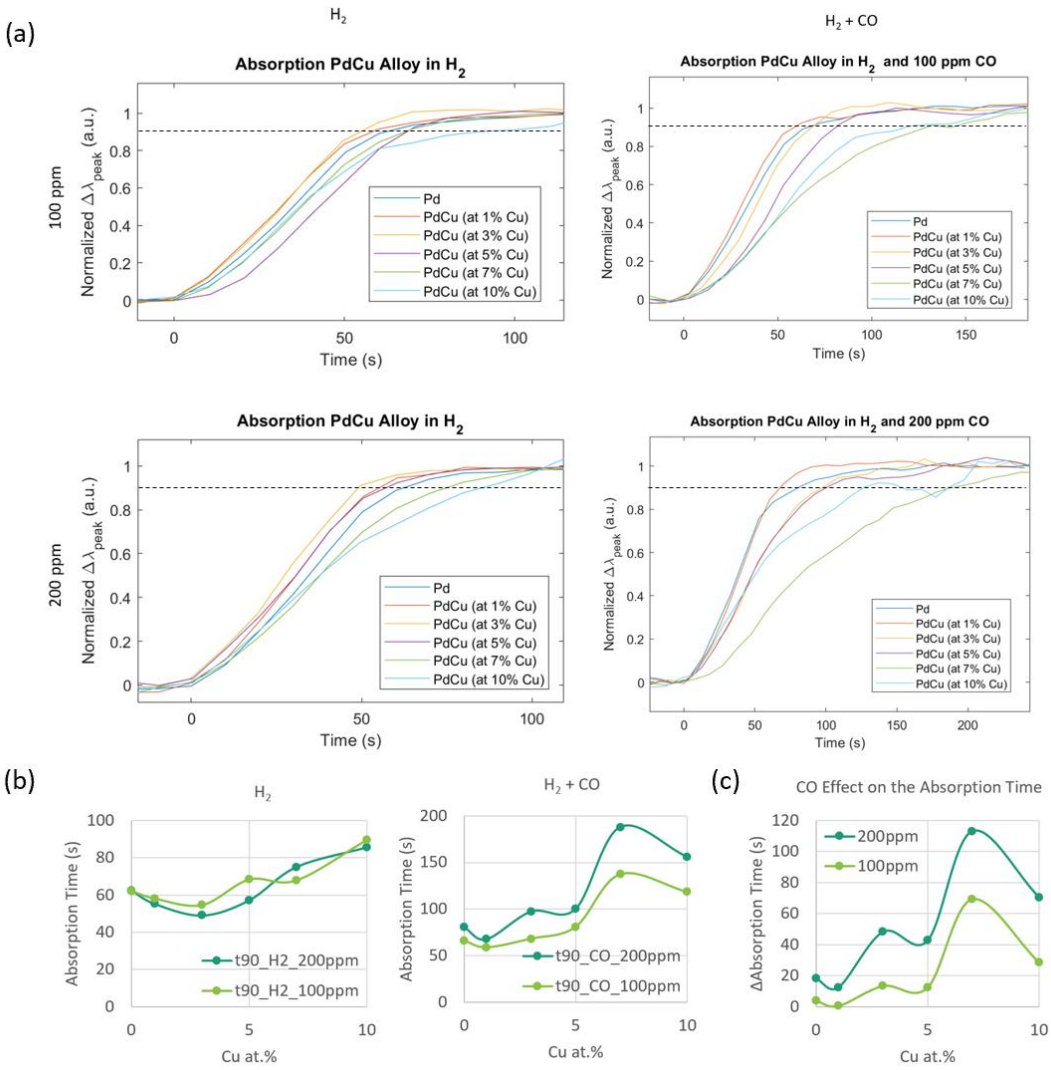

Figure 6.4 (a) Temporal response (normalized $\Delta\lambda_{peak}$) of PdCu-alloy sensors to stepwise hydrogen concentration (0 → 3.0 vol.%) without and with (100 and 200 ppm) CO background. The hydrogen pulse starts at t = 0. The dashed lines mark the 90% level of the maximum response. (b) The obtained absorption time, defined as t_{90}, as function of Cu compositions. (c) Time difference between the absorption time obtained in the CO and non-CO condition (b). The connecting-lines in (b) and (c) are guide to eyes.

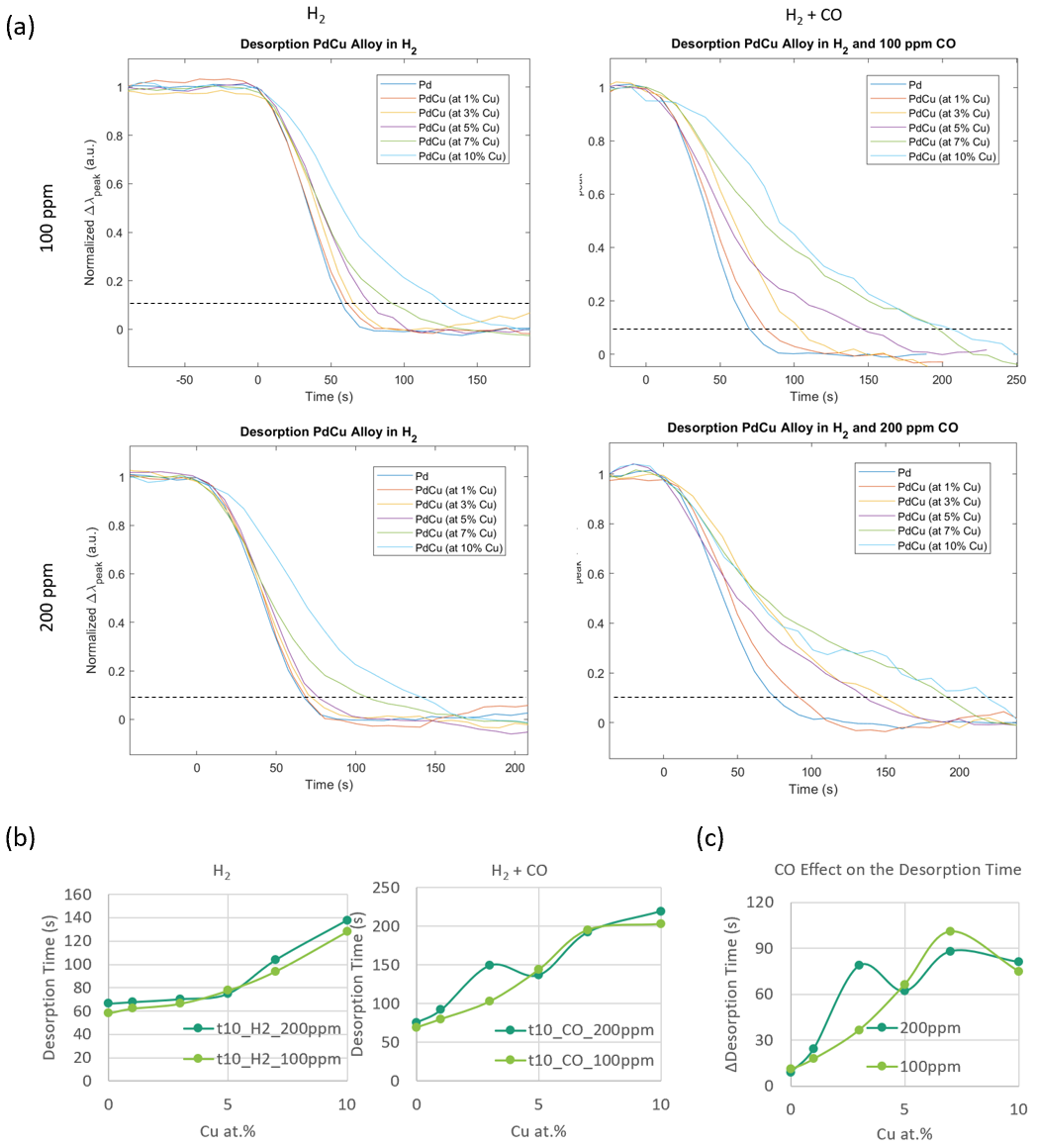

Figure 6.5 (a) Temporal response (normalized $\Delta\lambda_{peak}$) of the PdCu-alloy sensors to stepwise hydrogen concentration (3.0 → 0 vol.%) without and with (100 and 200 ppm) CO background. The hydrogen pulse starts at t = 0. The dashed lines mark the 10% level of the maximum response. (b) The obtained desorption time, defined as t_{10}, as function of Cu compositions. (c) Time difference between the absorption time obtained in the CO and non-CO condition (b). The connecting-lines in (b) and (c) are guide to eyes.

To quantitatively analyze the effect of CO background to the PdCu-alloy sensors (de)absorption kinetic, I select the response in 100 and 200 ppm CO background from Figure 6.2, because the response is saturated in the given exposure time. The normalized $\Delta\lambda_{peak}$ of the alloys during the hydrogen (de)absorption is presented in Figure 6.4a and Figure 6.5a and the calculated (de)absorption time are summarized in Figure 6.4b and Figure 6.5b. The absorption time is defined as t_{90}, (the time required to reach 90% of the maximum signal) and the desorption time is defined as t_{10} (the time required to reach 10% of the maximum signal).

There are several observations to highlight from the analysis:

(i) It is evident that the CO decelerates the absorption and desorption time, where the deceleration effect is weaker in 100 ppm than that in 200 ppm CO background. This is a consequence of more CO adsorption on the alloy's surface when the CO concentration is higher.

(ii) In the CO-free condition, the hydrogen absorption and desorption time are slower with increasing Cu content (Figure 6.4b and Figure 6.5b). The slow absorption and desorption time might have been a consequence of less Pd concentration in the PdCu alloy, which limits the hydrogen dissociation sites. In the case of the absorption, smaller hydrogen diffusivity and solubility in PdCu alloy[30] might have also contributed the slow absorption time since it is known that absorption is a diffusion limited process in Pd nanoparticle. Furthermore, in the CO background condition, both hydrogen absorption and desorption time are also slower with increasing Cu content.

(iii) To observe the CO effect on the (de)absorption time, I substracted the (de)absorption time measured in the CO and CO-free condition from panel (b) in Fig. 6.4 and 6.5, respectively. These substractions are presented in Fig. 6.4 (c) for absorption Fig. 6.5 (c). In both absorption and desorption processes, there seems to be oscillating correlation between the Cu content and the kinetics. It is also interesting that the global trend also shows that the CO deceleration effect is actually larger in the alloy with higher Cu concentration.

6.3 Optimizing the Pressure-Optical Response Isotherm

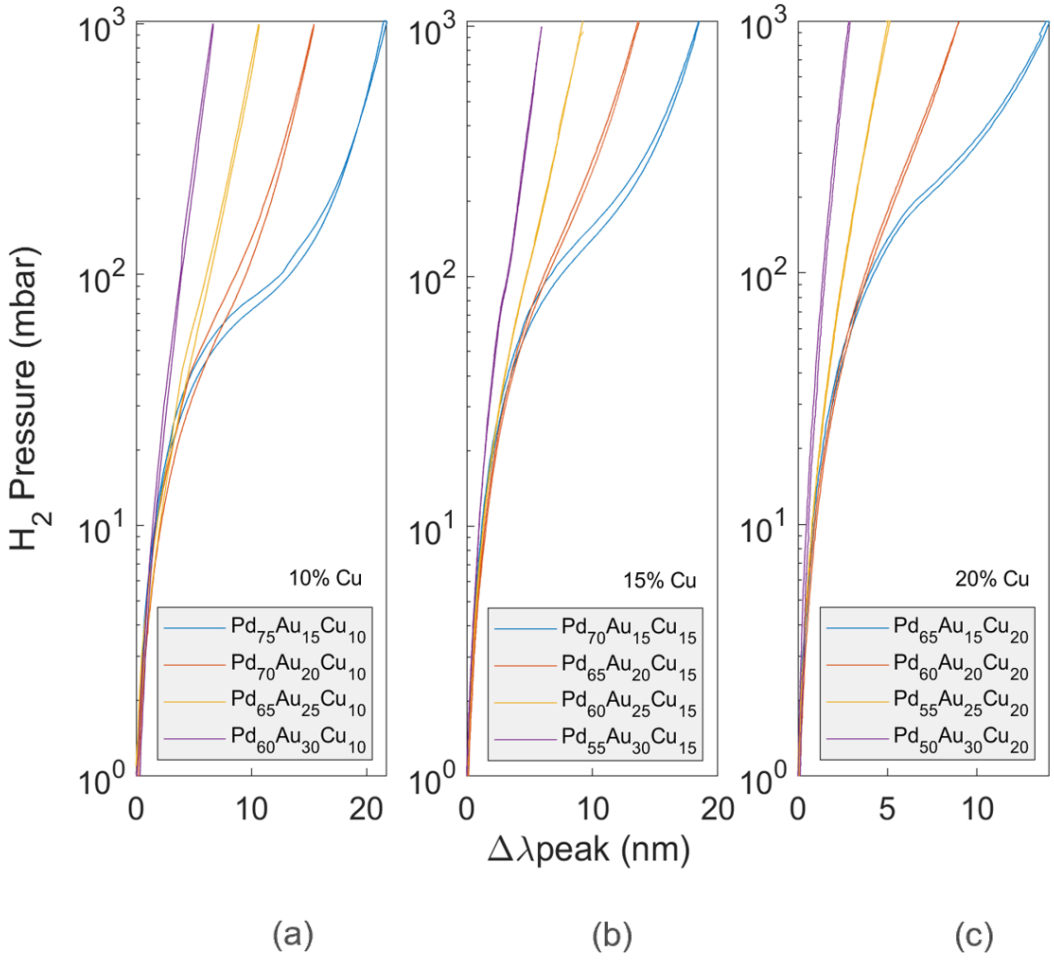

Figure 6.6 Pressure-$\Delta\lambda_{peak}$ isotherm of the PdAuCu ternary alloys. Each panel represents alloy with constant Cu at.% (10 (a), 15 (b), and 20 at.% (c)) with varying Au content of 15-30 at.%.

The CO-poisoning test presented in the previous section revealed that 10 at.% Cu is the minimum limit to protect the PdCu sensor in 500 ppm CO background. Accordingly, I introduced 10, 15, and 20 at.% of Cu in the PdAuCu ternary alloy. Furthermore, previous study on binary PdAu alloy suggest that minimum Au content to achieve hysteresis-free isotherm is 25 at.%. Therefore, for the PdAuCu isotherm optimization, I varied the Au concentration around that nominal.

The pressure-$\Delta\lambda_{peak}$ isotherm of the PdAuCu ternary alloy sensors is shown in Figure 6.6. Each panel shows isotherms of the alloy with constant Cu composition and varying Au composition from 15 to 30 at.%. Overall, the first order transition is still visible in the 15 at.% Au sensors, but the transition disappears at > 20 at.% Au. The hysteresis-free response is achieved by relatively low Au concentration (20 at.%) compared to that in PdAu binary system, which is 25-30 at.%, which implies the Cu's assistance to suppress hysteresis in the ternary sensors. Furthermore, it is also evident that higher Au concentration leads to reduced isotherm width ($\Delta\lambda$@1000 mbar-$\Delta\lambda$@1 mbar).

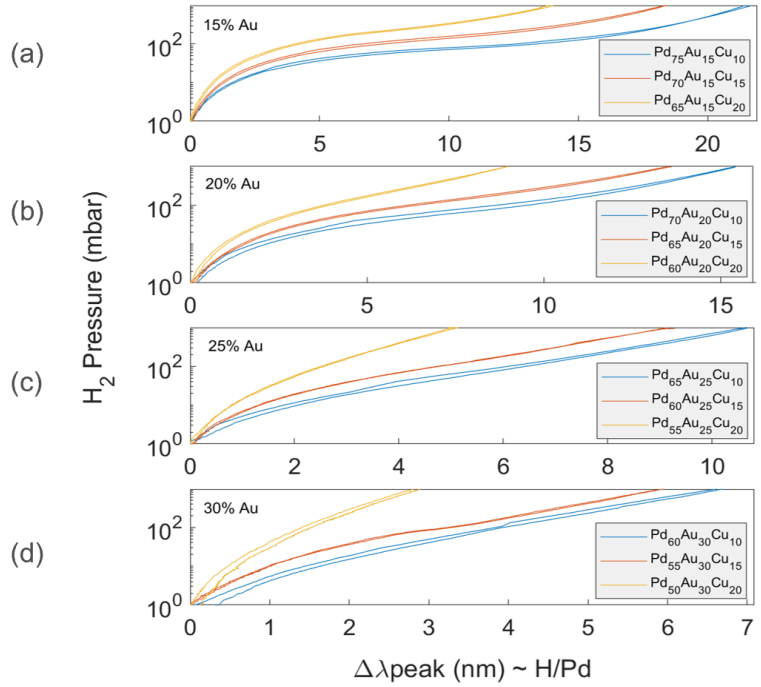

Figure 6.7 Pressure-$\Delta\lambda_{peak}$ isotherm of PdAuCu ternary alloy. Each panel represents alloy with constant Au at.% (15 (a), 20 (b), 25 (c), and 30 at.% (d)) with varying Cu content of 10-20 at.%.

To provide different perspective, the isotherms in Figure 6.6 is replotted at constant Au in Figure 6.7. It is interesting that the isotherm profile (shape) of different Cu concentrations are similar when Au is hold constant. This indicates that the isotherm shape is independent to the Cu but is dictated by the Au. Cu, on the other hand, induces the plateau elevation towards higher pressure, which is apparent in 15 at.% Au set of sensors. Figure 6.7a in agreement with the trend observed in the PdCu binary systems[8].

There are three criteria to assess the sensor isotherm to find the optimized one: (i) absence of hysteresis gap, (ii) absence of phase transition (related to the sensor's linearity), and (iii) the width of the overall isotherm (related to the sensor's overall sensitivity). For point (i), it is evident that the minimum Au concentration where the hysteresis is just about to close is 15 at.% (Figure 6.6). For point (ii), linear response is achieved when the Au concentration is 25 and 30 at.% (Figure 6.6). However, according to point (iii), 25 at.% is a more reasonable choice since the 30 at.% Au has narrower isotherm signals (Figure 6.7). And finally, point (iii) prevents the use of higher Cu concentration since Cu tends to reduce the sensor's sensitivity. Therefore, from those assessment points, the champion systems are $Pd_{60}Au_{25}Cu_{15}$ and $Pd_{65}Au_{25}Cu_{15}$.

6.4 Absorption and Desorption Time of the PdAuCu Alloy Sensors

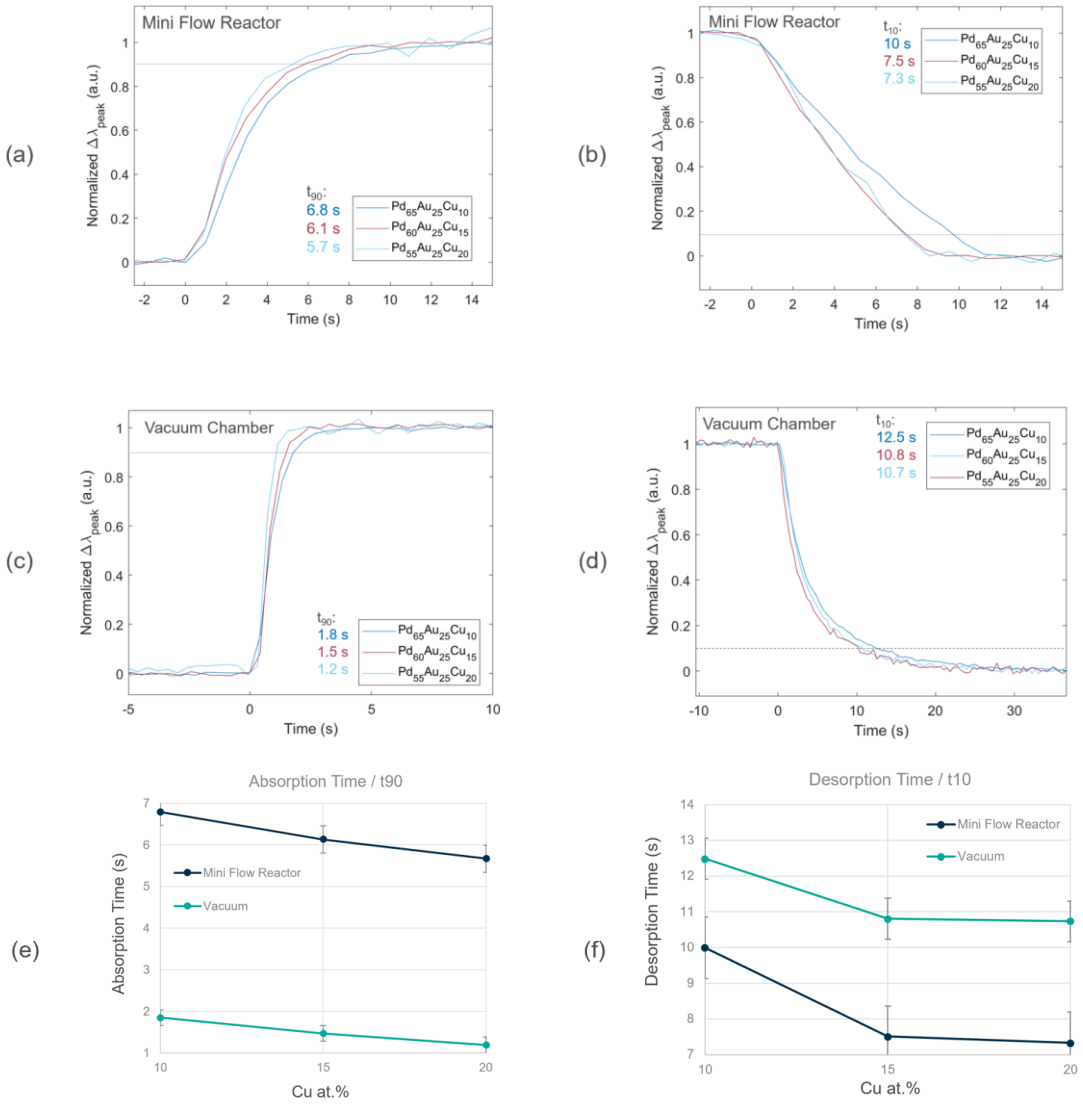

Figure 6.8 Absorption and desorption kinetics of $Pd_{65}Au_{25}Cu_{10}$, $Pd_{60}Au_{25}Cu_{15}$, and $Pd_{55}Au_{25}Cu_{20}$ measured in mini flow reactor (a,b, respectively) and in vacuum chamber (c, d, respectively). The dashed lines mark the 90 % and 10% level of the maximum response for the absorption and the desorption, respectively. The kinetic were measured in 3.5% H_2 in synthetic air carrier for the mini flow reactor and in 35 mbar H_2 pressure for the vacuum chamber at same temperature 25°C. The calculated t_{90} and t_{10} are plotted in e and f, respectively.

The absorption and desorption kinetics of the champion systems measured in the mini flow reactor (3.5 vol.% H_2 in synthetic air) and in the vacuum chamber (25 mbar H_2 pressure) are presented in Figure 6.8. In the reactor and the chamber, both absorption (t_{90}) and desorption time (t_{10}) show decreasing trend as the Cu concentration increases (e and f, respectively). The decreasing trend might have been consequence of lower hydrogen (de)absorption apparent activation energy[32].

In addition, there is discrepancy in the recorded absorption and desorption time in measured in the mini flow reactor and the vacuum chamber. For the absorption kinetics, the measurement in vacuum chamber shows faster response than that in the mini flow reactor. The faster response might have been due to the fact that hydrogen in the vacuum chamber is static while in the mini flow reactor is dynamic. This leads to faster hydrogen capture by the alloy nanoparticles in the vacuum chamber than in the mini flow reactor. Moreover, the slower hydrogen absorption in the mini flow reactor could also have been the effect of hydrogen dilution in synthetic air carrier, which leads to slower diffusion to the alloy nanoparticle surface.

On the other hand, the recorded desorption kinetic is faster in the mini flow reactor than in the vacuum reactor. This could have been caused by the synthetics air flow which assists the hydrogen desorption from the alloy nanoparticle surface. It is also worth to note that the desorption signal profiles are different between the vacuum and mini-flow reactor (Fig 6.8). In the mini-flow reactor, there was a sudden change of rate before the signal reach the baseline while for the vacuum system, which indicates different rate-limiting factor.

6.5 Effect of the Carrier Gas

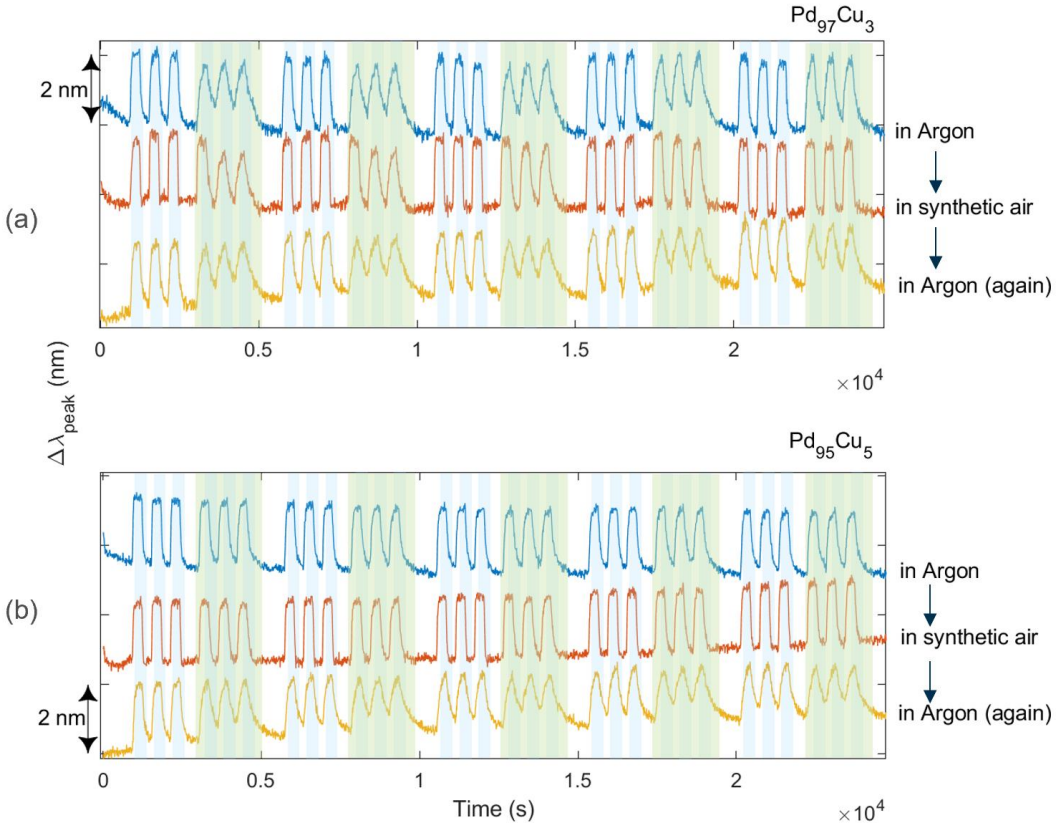

Figure 6.9 Temporal response ($\Delta\lambda_{peak}$) of (a) PdCu (3 at.%) and (b) PdCu (5 at.%) alloys in Ar and synthetic air carrier. The test was done subsequently in Ar carrier gas, in synthetic air and finally in Ar again.

In Figure 6.2, I found that the effect of 100 ppm CO poisoning to pure Pd sensor was not that noticeable, which is in contrast to the claim that few ppm of CO is sufficient to deactivate Pd[33]. The subtle CO poisoning effect might have been due to the Pd alloy's catalytic effect which oxidizes CO in the presence of O_2 (of synthetic air)[31]. To further investigate this hypothesis, I performed the sensing tests of the freshly

made $Pd_{95}Cu_5$ and $Pd_{97}Cu_3$ subsequently in Ar, synthetic air, and in Ar again (Figure 6.9).

From the tests, there several remarks to highlight:

(i) The assistance of the synthetic air to alleviate the CO poisoning effect is obvious as indicated by the slower response of the alloys when measured in Ar than that in synthetic air. This corroborates the Pd's catalytic effect to oxidize CO, which reduces the CO poisoning effect.

(ii) The synthetic air induces irreversible effect to the alloys as indicated by the different response in the first and second Ar tests. The synthetic air might have induced a surface segregation or oxidation to the alloy. The effect of the synthetic air is quite severe that in the second Ar test, the sensor's response did not even saturate when CO background is removed, which indicates the presence of accumulated adsorbed CO on the alloy surface.

7. Conclusion and Outlook

Investigation of the composition-dependent response of palladium-alloy-based plasmonic hydrogen sensors has been conducted. The inherent hysteresis and CO poisoning shortcomings in the Pd has been addressed with Au and Cu alloying, respectively. There are several key points to summarize:

- Poisoning resistance test in 500 ppm CO background revealed that minimum 10 at.% of Cu is required to promote CO-poisoning resistance PdAuCu alloy sensor.

- Hysteretic-free and linear response were achieved when the Au concentration is at least 25 at.%.

- The champion systems, $Pd_{65}Au_{25}Cu_{10}$ and $Pd_{65}Au_{25}Cu_{15}$, show reasonably fast response time of 6.8 and 6.1 s; and recovery time of 10.0 ad 7.5 s, respectively at room temperature and in synthetic air background for 3.5 % H_2.

As an outlook, there are several interesting aspects to pursue in the future:

- The optimized sensor has exhibited excellent performances, but the response and recovery time is still behind the DOE standard. Further improvement can be achieved by reducing the nanoparticle size or coating with polymer.

- The test in Ar and synthetic air background revealed instability of the alloy. Further investigation on the gas effect to the alloy stability will provide more insight that is also useful for application perspective.

8. References

1. Crabtree, G. W., Dresselhaus, M. S. & Buchanan, M. V. Hydrogen: The Fuel of the Future? *Basic Choices Constraints Long-Term Energy Supplies Phys. Today* **57**, 47 (2004).

2. D, Fraile; J, Lanoix; P, Maio; A, Rangel; A, T. *'Needs and benefits of "green" hydrogen in light of a market outlook'*. (2015).

3. Buttner, W. *et al. Hydrogen Safety Sensor Performance and Use Gap Analysis: Preprint*. www.nrel.gov/publications. (2007).

4. Hübert, T., Boon-Brett, L., Black, G. & Banach, U. Hydrogen sensors - A review. *Sensors and Actuators, B: Chemical* vol. 157 329–352 (2011).

5. Linic, S., Christopher, P. & Ingram, D. B. Plasmonic-metal nanostructures for efficient conversion of solar to chemical energy. (2011) doi:10.1038/NMAT3151.

6. Wadell, C., Syrenova, S. & Langhammer, C. Plasmonic Hydrogen Sensing with Nanostructured Metal Hydrides. **12**, 28 (2020).

7. Wadell, C. *et al.* Hysteresis-free nanoplasmonic pd-au alloy hydrogen sensors. *Nano Lett.* (2015) doi:10.1021/acs.nanolett.5b01053.

8. Darmadi, I., Nugroho, F. A. A., Kadkhodazadeh, S., Wagner, J. B. & Langhammer, C. Rationally Designed PdAuCu Ternary Alloy Nanoparticles for Intrinsically Deactivation-Resistant Ultrafast Plasmonic Hydrogen Sensing. *ACS Sensors* **4**, 1424–1432 (2019).

9. Nugroho, F. A. A., Iandolo, B., Wagner, J. B. & Langhammer, C. Bottom-Up Nanofabrication of Supported Noble Metal Alloy Nanoparticle Arrays for Plasmonics. *ACS Nano* **10**, 2871–2879 (2016).

10. Sinclair, I. R. Chapter 3 - Light and associated radiation. in (ed. Sinclair, I. R. B. T.-S. and T. (Third E.) 53–86 (Newnes, 2001). doi:https://doi.org/10.1016/B978-075064932-2/50023-0.

11. Fredriksson, H. *et al.* Hole–Mask Colloidal Lithography. *Adv. Mater.* **19**, 4297–4302 (2007).

12. *Optical Properties of Plasmonic Materials*.

13. Palm, K. J., Murray, J. B., Narayan, T. C. & Munday, J. N. Dynamic optical properties of metal hydrides. *ACS Photonics* **5**, 4677–4686 (2018).

14. Anggoro, F. & Nugroho, A. *Nanoplasmonic Alloy Hydrogen Sensors A Quest for Fast, Sensitive and Poisoning-Resistant Hydrogen Detection*.

15. Cattania, M. G., Penka, V., Behm, R. J., Christmann, K. & Ertl, G. Interaction of hydrogen with a palladium (110) surface. *Surf. Sci.* **126**, 382–391 (1983).

16. Langhammer, C., Zhdanov, V. P., Zorić, I. & Kasemo, B. Size-dependent hysteresis in the formation and decomposition of hydride in metal nanoparticles. *Chem. Phys. Lett.* **488**, 62–66 (2010).

17. Darmadi, I. Palladium-Based Nanoplasmonics for Ultrafast and Deactivation-Resistant Hydrogen Detection. *PQDT - Glob.* 90 (2019).

18. Knapton, A. G. Palladium Alloys for Hydrogen Diffusion Membranes. *Platin. Met. Rev.* **21**, 44–50 (1977).

19. *Hydrogen in Metals II*. vol. 29 (Springer Berlin Heidelberg, 1978).

20. Schwarz', R. B. & Khachaturyan', A. G. *Thermodynamics of Open Two-Phase Systems with Coherent Interfaces*. vol. 74 (1995).

21. Fisser, M., Badcock, R. A., Teal, P. D. & Hunze, A. Optimizing the sensitivity of palladium based hydrogen sensors. *Sensors Actuators, B Chem.* **259**, 10–19 (2018).

22. Sengar, S. K. & Mehta, B. R. Size and alloying induced changes in lattice constant, core, and valance band binding energy in Pd-Ag, Pd, and Ag nanoparticles: Effect of in-flight sintering temperature. *J. Appl. Phys* **112**, 14307 (2012).

23. Manchester, F. D., San-Martin, A. & Pitre, J. M. *Section 11: Phase Diagram Evaluations The H-Pd (Hydrogen-Palladium) System Equilibrium Diagram*.

24. Allison, E. G. & Bond, G. C. Catalysis Reviews The Structure and Catalytic Properties of Palladium-Silver and Palladium-Gold Alloys The Structure and Catalytic Properties of Palladium-Silver and Palladium-Gold Alloys. (1973) doi:10.1080/01614947208062259.

25. Subramanlan, P. R. & Laughlin, D. E. *Phase Diagram Evaluations: Section II Cu-Pd (Copper-Palladium).*

26. Das, R. & Chanda, A. Fabrication and properties of spin-coated polymer films. in *Nano-Size Polymers: Preparation, Properties, Applications* 283–306 (Springer International Publishing, 2016). doi:10.1007/978-3-319-39715-3_10.

27. Norrman, K., Ghanbari-Siahkali, A. & Larsen, N. B. Studies of spin-coated polymer films. *Annual Reports on the Progress of Chemistry - Section C* vol. 101 174–201 (2005).

28. Vaideki, K. Plasma technology for antimicrobial textiles. in *Antimicrobial Textiles* 73–86 (Elsevier Inc., 2016). doi:10.1016/B978-0-08-100576-7.00005-5.

29. Nugroho, F. A. A., Darmadi, I., Zhdanov, V. P. & Langhammer, C. Universal Scaling and Design Rules of Hydrogen-Induced Optical Properties in Pd and Pd-Alloy Nanoparticles. *ACS Nano* **12**, 9903–9912 (2018).

30. Perrot, P. *Copper-Hydrogen-Palladium*. (2006).

31. Kim, H. Y. & Henkelman, G. CO adsorption-driven surface segregation of Pd on Au/Pd bimetallic surfaces: Role of defects and effect on CO oxidation. *ACS Catal.* **3**, 2541–2546 (2013).

32. O'Brien, C. P. & Lee, I. C. The interaction of CO with PdCu hydrogen separation membranes: An operando infrared spectroscopy study. *Catal. Today* (2017) doi:10.1016/j.cattod.2017.09.039.

33. Evaluation of selectivity of commercial hydrogen sensors. *Int. J. Hydrogen Energy* **39**, 20491–20496 (2014).

DEPARTMENT OF PHYSICS
DIVISION OF CHEMICAL PHYSICS
CHALMERS UNIVERSITY OF TECHNOLOGY
Gothenburg, Sweden
www.chalmers.se

CHALMERS
UNIVERSITY OF TECHNOLOGY